JGR Solid Earth

RESEARCH ARTICLE
10.1029/2021JB022250

Analyzing Explosive Volcanic Deposits From Satellite-Based Radar Backscatter, Volcán de Fuego, 2018

E. W. Dualeh[1], S. K. Ebmeier[1], T. J. Wright[1], F. Albino[2], A. Naismith[2], J. Biggs[2], P. A. Ordoñez[3], R. M. Boogher[3], and A. Roca[3]

[1]COMET, School of Earth and Environment, University of Leeds, Leeds, UK, [2]COMET, School of Earth Sciences, University of Bristol, Bristol, UK, [3]Instituto Nacional de Sismología, Vulcanología, Meteorología e Hidrología (INSIVUMEH), Guatemala City, Guatemala

Key Points:

- Radar backscatter observed 3 pyroclastic density currents and 9 periods of lahar activity in a single drainage system between January and October 2018
- Backscatter noise is reduced by up to 42% by using dense time series, which aids in the extraction of subtle signals in explosive deposits
- Backscatter corrections and understanding of pre-eruption scattering properties are necessary for meaningful analysis of explosive deposits

Supporting Information:

Supporting Information may be found in the online version of this article.

Correspondence to:

E. W. Dualeh,
eeewd@leeds.ac.uk

Citation:

Dualeh, E. W., Ebmeier, S. K., Wright, T. J., Albino, F., Naismith, A., Biggs, J., et al. (2021). Analyzing explosive volcanic deposits from satellite-based radar backscatter, Volcán de Fuego, 2018. *Journal of Geophysical Research: Solid Earth*, *126*, e2021JB022250. https://doi.org/10.1029/2021JB022250

Received 21 APR 2021
Accepted 9 SEP 2021

Abstract Satellite radar backscatter has the potential to provide useful information about the progression of volcanic eruptions when optical, ground-based, or radar phase-based measurements are limited. However, backscatter changes are complex and challenging to interpret: explosive deposits produce different signals depending on pre-existing ground cover, radar parameters and eruption characteristics. We use high temporal- and spatial-resolution backscatter imagery to examine the emplacement and alteration of pyroclastic density currents (PDCs), lahar and ash deposits from the June 2018 eruption of Volcán de Fuego, Guatemala, using observatory reports and rainfall gauge data to ground truth our observations. We use a temporally dense time series of backscatter data to reduce noise and extract deposit areas. We observe backscatter changes in six drainages, the largest deposit was 11.9-km-long that altered an area of 6.3 km^2 and had a thickness of 10.5 ±2 m in the lower sections as estimated from radar shadows. The 3 June eruption also produced backscatter signal over an area of 40 km^2, consistent with reported ashfall. We use transient patterns in backscatter time series to identify nine periods of high lahar activity in a single drainage system between June and October 2018. We find that the characterization of subtle backscatter signals associated with explosive eruptions are best observed with (1) radiometric terrain calibration, (2) speckle correction, and (3) consideration of pre-existing scattering properties. Our observations demonstrate that SAR backscatter can capture the emplacement and subsequent alteration of a range of explosive deposits, allowing the progression of an explosive eruption to be monitored.

Plain Language Summary Volcanic eruptions cause changes to the Earth's surface that can be observed using satellite-based radar instruments. Changes to the radar scattered back from the surface can be caused by new volcanic deposits or changes to the ground caused by an eruption. However, such signals are also affected by what was there before the eruption and variations in the satellite positions. Deposits from explosive eruptions are particularly hard to identify because they can affect radar signals in different ways. We use a high spatial and temporal resolution satellite radar dataset to identify different volcanic deposits from the June 2018 eruption of Volcán de Fuego, Guatemala. We were able to identify three types of volcanic deposit from radar backscatter: hot mixture of solid particle and gas (pyroclastic density currents), water saturated flow with solid particles (lahars), and ash. We observe backscatter changes over six drainage systems that were affected by pyroclastic density currents in June 2018. Combining our radar dataset with rainfall data, we identify nine periods of lahars in one drainage between June and October 2018. We describe what information and corrections are helpful to identify volcanic changes in backscatter and especially to monitor the progression of an explosive eruption.

1. Introduction

During an explosive volcanic eruption, monitoring can be impeded by both cloud coverage and damage to instrument networks. However, satellite-based Synthetic Aperture Radar (SAR) images are unaffected by cloud and can provide frequent observations during an eruption. While measurements from differential Interferometric Synthetic Aperture Radar (InSAR) are increasingly used for volcano monitoring (e.g., Ebmeier et al., 2018; Fournier et al., 2010; Pritchard et al., 2018), radar backscatter from individual SAR images (e.g., Wadge et al., 2011, 2012) is still under-exploited. Backscatter changes can have a high magnitude and easy to identify (e.g., dome collapse, Pallister et al., 2013), or very subtle (e.g., ash dispersion, Arnold et al., 2018).

The interpretation of SAR backscatter for volcanology is challenging because there is no simple relationship between the magnitude or sign of backscatter change and the physical properties of fresh volcanic deposits. Backscatter signals from explosive deposits are particularly difficult to interpret because their thickness varies over several orders of magnitude and because of their tendency to be rapidly remobilized and eroded.

We use imagery spanning the June 3, 2018 eruption of Volcán de Fuego (Albino et al., 2020; INSIVUMEH, 2018d; Pardini et al., 2019) to investigate the potential of backscatter for monitoring explosive eruptions. We characterize the backscatter changes associated with the initial emplacement of PDC deposits and ash fallout and investigate the post-eruption remobilization of material through lahars in the subsequent 4 months.

1.1. Monitoring Volcanic Processes Using Synthetic Aperture Radar Backscatter

The proportion of the transmitted electromagnetic pulse that the ground directs back toward the satellite (i.e., backscatter) is described as the Radar Cross Section (RCS), σ. For a calibrated SAR image, a single pixel covers an area that includes multiple scatterers and as shown in Flores-Anderson et al. (2019) can be expressed as,

$$\sigma^{\circ} = \frac{4\pi R^2 \rho_R}{\rho_T A} \quad (1)$$

where σ° is the normalised RCS, ρ_T and ρ_R are the power density (Wm^{-2}) scattered by the sensor and received by the target respectively, R is the distance or range between sensor and target, and A is the pixel surface area. σ° is also described as the backscatter coefficient can be extracted from the raw data provided by the satellite and is sensitive to changes in the satellite parameters, which are the local incidence angle, wavelength λ and polarisation (i.e., the orientation of the oscillation plane for a wave, Flores-Anderson et al., 2019) and the scattering properties of the ground. Variables including surface roughness, local slope, and dielectric properties are combined to determine the scattering properties of the ground surface. Backscatter signals vary between tracks and satellites based on difference in the satellite viewing geometry and pixel resolution. Erupted material may alter one or all of these scattering properties, which are also affected by independent non-volcanic processes such as rainfall, producing complex backscatter signals. For volcanic deposits, the surface roughness generally contributes the most change to the radar backscatter signal recorded. Conventionally, due to its high dynamic range the radar backscatter is expressed in decibels ($\sigma^{\circ}_{dB} = 10\log_{10}\sigma^{\circ}$).

Over the last two decades, multiple studies have used SAR backscatter to observe volcanic eruptions (Table 1). These have included measurements of dome growth (e.g., Pallister et al., 2013; Wadge et al., 2011), mapping of fresh lavas (e.g., Arnold et al., 2017; Wadge et al., 2012), extracting lava lake heights (e.g., Barrière et al., 2018; Moore et al., 2019) and flow thicknesses (Arnold et al., 2017; Wadge et al., 2012) measured using radar shadows.

Explosive volcanic deposits are more challenging to analyze in backscatter, but major PDCs have been identified both in single backscatter images (Carn, 1999) and using multi-image composites (Wadge et al., 2011). Finer and more widespread volcanic deposits such as ash fallout produce subtle backscatter changes. Four studies have identified ash deposits (Arnold et al., 2018; Goitom et al., 2015; Meyer et al., 2015; Wadge & Haynes, 1998) and show that signals are strongly related to the pre-existing surface roughness and whether ash infills and smooths the surface on the scale of the satellite wavelength, or changes a specular reflecting surface (e.g., ice) to one that scatters diffusely (e.g., Arnold et al., 2018).

1.2. The 2018 Eruption of Volcán de Fuego, Guatemala

Volcán de Fuego (3763 m a.s.l.) is the southernmost and currently most active crater of the Fuego-Acatenango volcanic complex in Guatemala, located ~ 40 km southwest of the capital, Guatemala City. Since the first written record of activity at Fuego in 1524, the volcano has had ~ 60 subplinian eruptions (Global Volcanism Program & Wunderman, 2005) separated by long periods of intermittent Strombolian activity, making it one of the most active volcanoes in Central America. Periods of high activity at Fuego are characterized by frequent Strombolian eruptions, producing short lava flows (100's m), lahars and ash explosions (Lyons

Table 1
Summary of Previous Case Studies Using Backscatter to Examine Volcanic Deposits

	Volcano	Study timespan	Process	Methods used	References
Explosive eruptions	Mt. Unzen, Japan	1991–1995	Pyroclastic flow	Differences image[a]	Terunuma et al. (2005)
			Lahars		
	Pinatubo, Philippines	1993	Lahars	Single image examination[b]	Carr et al. (2007)
	East Java Volcanoes	1995	Pyroclastic flow	Single image examination[b]	Carn (1999)
			Lahars		
			Dome activity		
	Soufiere Hills, Montserrat	1996	Pyroclastic flow	Composite image[c]	Wadge and Haynes (1998)
			Ash		
		1996–1999	Pyroclastic flow	Ratio maps[a]	Wadge et al. (2002)
			Dome activity		
		2008–2010	Pyroclastic flow	Single image examination[b]	Wadge et al. (2011)
			Lahars	RGB color maps[c]	
			Dome activity	Radar shadows[d]	
	Okmok, USA	2008	Ash	Ratio maps[a]	Meyer et al. (2015)
	Merapi, Indonesia	2010	Pyroclastic flow	Single image examination[b]	Pallister et al. (2013)
			Dome activity		
			Pyroclastic flow	Single image examination[b]	Solikhin et al. (2015)
			Tephra	Ratio maps[a]	Saepuloh et al. (2010)
			Pyroclastic flow	Ratio maps[a]	Saepuloh et al. (2015)
	Cotapaxi, Ecuador	2015	Ash	Single image examination[b]	Arnold et al. (2018)
			Crater morphology	RGB color maps[c]	
	Anak Krakatau, Indonesia	2018	Flank collapse	Single image examination[b]	Walter, Haghighi, et al. (2019) and Williams et al. (2019)
Effusive eruptions	Bagana, Papua New Guinea	2010–2011	Lava flows	RGB color maps[c]	Wadge et al. (2012)
				Radar shadows[d]	
	Stromboli, Italy	2010–2014	Lava flows	RGB color maps[c]	Di Traglia et al. (2018)
			Slope failure		
	Nabro, Eritrea	2011	Tephra	Normalised difference[c]	Goitom et al. (2015)
			Lava flow	Single image examination[b]	
				Radar shadows[d]	
	Shinmoe-dake, Japan	2011	Dome growth	Single image examination[b]	Ozawa and Kozono, (2013)
	El Reventador, Ecuador	2011–2016	Lava flows	Single image examination[b]	Arnold et al. (2017)
			Dome activity	Radar shadows[d]	
	Tolbachik, Kamchatka	2012–2013	Lava flows	Single image examination[b]	Kubanek et al. (2017)
				Normalised difference[c]	
	Colima, Ecuador	2013	Dome Activity	Single image examination[b]	Walter, Harnett, et al. (2019)
				RGB color maps[c]	
	Holuhraun, Iceland	2014–2015	Lava flows	Single image examination[b]	Pedersen et al. (2017)
					Dumont et al. (2018)
	Erta 'Ale, Ethiopia	2017	Lava lake fluctuations	Radar shadows[d]	Moore et al. (2019)

Table 1
Continued

	Volcano	Study timespan	Process	Methods used	References
Others	Cordón Caulle, Chile	2011–2012	Laccolith Intrusion	Single image examination[b]	Castro et al. (2016)
			Lava flow		Delgado et al. (2019)
	Mount Cleveland, Alaska	2011–2012	Dome activity	Single image examination[b]	Wang et al. (2015)
	Arenal, Costa Rica	2011–2013	Slope failure	RGB color maps[c]	Ebmeier et al. (2014)
	Nyiragongo, D.R. Congo	2016–2017	Lava lake fluctuations	Radar shadows[d]	Barrière et al. (2018)
	Kadovar, Papua New Guinea	2018–2019	Slope failure	Single image[b]	Plank et al. (2019)
			Peripheral Dome Growth	RGB color maps[c]	
			Lava Flow		

[a]pairwise comparison of two backscatter images (e.g., differencing, normalization, ratios etc.). [b]examining single backscatter images. [c]visualisation method using multiple backscatter images. [d]measuring heights using radar shadows.

et al., 2010; Patrick et al., 2007). These periods are interspersed with high magnitude explosive eruptions, known as paroxysms (Martin & Rose, 1981). These paroxysms are short lived (~ 24–48 h) eruptions that produce longer lava flows (100–1,000s m), PDCs, and are able to produce an eruptive column. Volcán de Fuego is monitored by INSIVUMEH (Instituto Nacional de Sismología, Vulcanologia, Meteorologia e Hidrología) from Guatemala, who are responsible for monitoring and communication on natural hazards, including volcanic activity, to the government and private sector.

The current period of activity started in 1999 (Lyons et al., 2010) with eruptive intensity increasing in 2015 (Naismith et al., 2019). The 3 June 2018 eruption was an unusually large paroxysm (Naismith et al., 2019), with much longer PDCs compared to previous eruptions and activity. The eruption began on June 3, 2018 at 06:00 local time with frequent strong summit explosions accompanied by PDCs and a plume that reached up to 17.5 km a.s.l (Pardini et al., 2019). The first PDCs were emplaced on the western flanks of the volcano (INSIVUMEH, 2018c). By 14:00 local time, PDCs had descended six drainage ravines on the east and west flanks. These included multiple flows inside Barranca Las Lajas (Figure 1). Most of the PDCs were restricted to the upper flanks of Fuego, ~4 km from summit. However, the series of PDCs in Barranca Las Lajas extended over 12 km from the summit, longer than all the other flows, and buried the town of San Miguel Los Lotes (Figure 1d), killing several hundreds of people. Official numbers report 332 people missing as a result of the eruption, although the death toll could be as high as 2,900 people (Naismith et al., 2020).

The eruption ended after 16 h, when activity was reduced to an ash column of ~4,500 m a.s.l (INSIVUMEH, 2018d) and weak to moderate explosions at the summit. Over the following days activity level remained high, with multiple PDCs recorded on the 5^{th}, 7^{th}, 8^{th}, and 12^{th} June, dominantly on the east flank of Fuego (INSIVUMEH, 2018a, 2018b, 2018e, 2018f). Interaction between the freshly deposited material and high levels of rainfall resulted in frequent lahars: INSIVUMEH reported 65 lahars between June 3 and July 1, 2018.

2. Backscatter Dataset

COSMO-SkyMed (CSK) is a constellation of four X-band (3.1 cm) satellites, with a 2 × 3 meters pixel dimensions in radar geometry in stripmap mode. We used 62 HH-polarised (horizontal transmit and horizontal receive) acquisitions from an ascending (H4-0B) and descending (H4-03) track between January and October 2018. This time frame includes (a) a typical Fuego paroxysm in February 2018, (b) the unusually large June 3, 2018 paroxysm, (c) three months prior to the 3 June paroxysm that were uncharacteristically quiet compared to recent activity and (d) four months after the eruption that encompassed smaller PDCs, multiple lahars and the transition from the dry to wet season. The wet season lasts between April and September, with a pause in rainfall during July, known as the canícula. Acquisition intervals range from 1 to 8 days, with an average perpendicular baseline (i.e., the distance between the satellite position at the time of acquisition perpendicular to the line of sight) of 690 m (ranging from 6 to 1890 m).

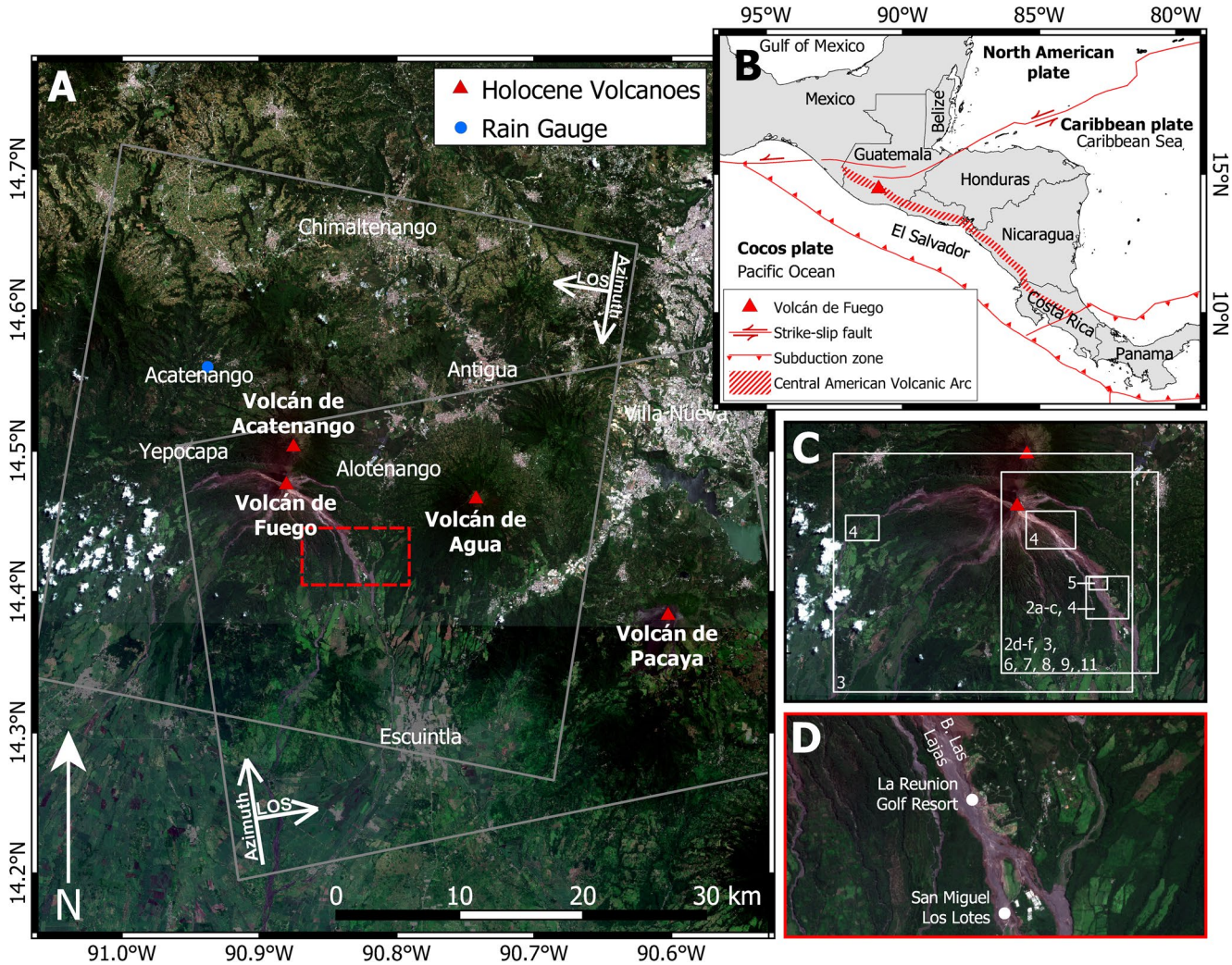

Figure 1. (a) Map of Volcán de Fuego showing the footprint of COSMO-SkyMed tracks and look direction (white rectangle), with (b) location of Fuego within Guatemala. (c) spatial extents used for subsequent figures in this article are shown by white outlines with corresponding figure number and (d) names of settlements and notable locations (Basemap: November 11, 2018 and July 04, 2018, Copernicus Sentinel-2 data).

2.1. Corrections and Calibrations

We produced full resolution geocoded backscatter images using the GAMMA remote sensing software (Werner et al., 2000), with the spatial extent of all images resampled to a common date to facilitate comparison. Slopes facing toward or away from a side-looking SAR sensor will appear in radar images to be either foreshortened or lengthened respectively. If the slope's gradient is steeper than the radar incidence angle, returns from the top of the slope reach the satellite before those from the bottom, producing a layover effect. Similarly, steep slopes facing away from the satellite cast a shadow, from which no information is scattered back to the SAR sensor. To mitigate the impact of topography on backscatter we make a terrain-based radiometric calibration (Figure 2c) using 10 m resolution digital elevation models (DEMs), constructed from pairs of TanDEM-X bistatic images acquired on October 18, 2015 and August 09, 2018 (Albino et al., 2020). The DEM has a vertical precision <5 m. However, due to the lack of ground control points (e.g., GPS measurements) for the area the vertical accuracy of the DEM could not be evaluated (Albino et al., 2020). The radiometric terrain correction uses the DEM to increase the accuracy of the pixel area estimation used in the normalization of the backscatter coefficient. The calibration also reduces the sensitivity to the incidence angle by normalizing the backscatter coefficient by the cosine of the incidence angle (Meyer et al., 2015; Small, 2011).

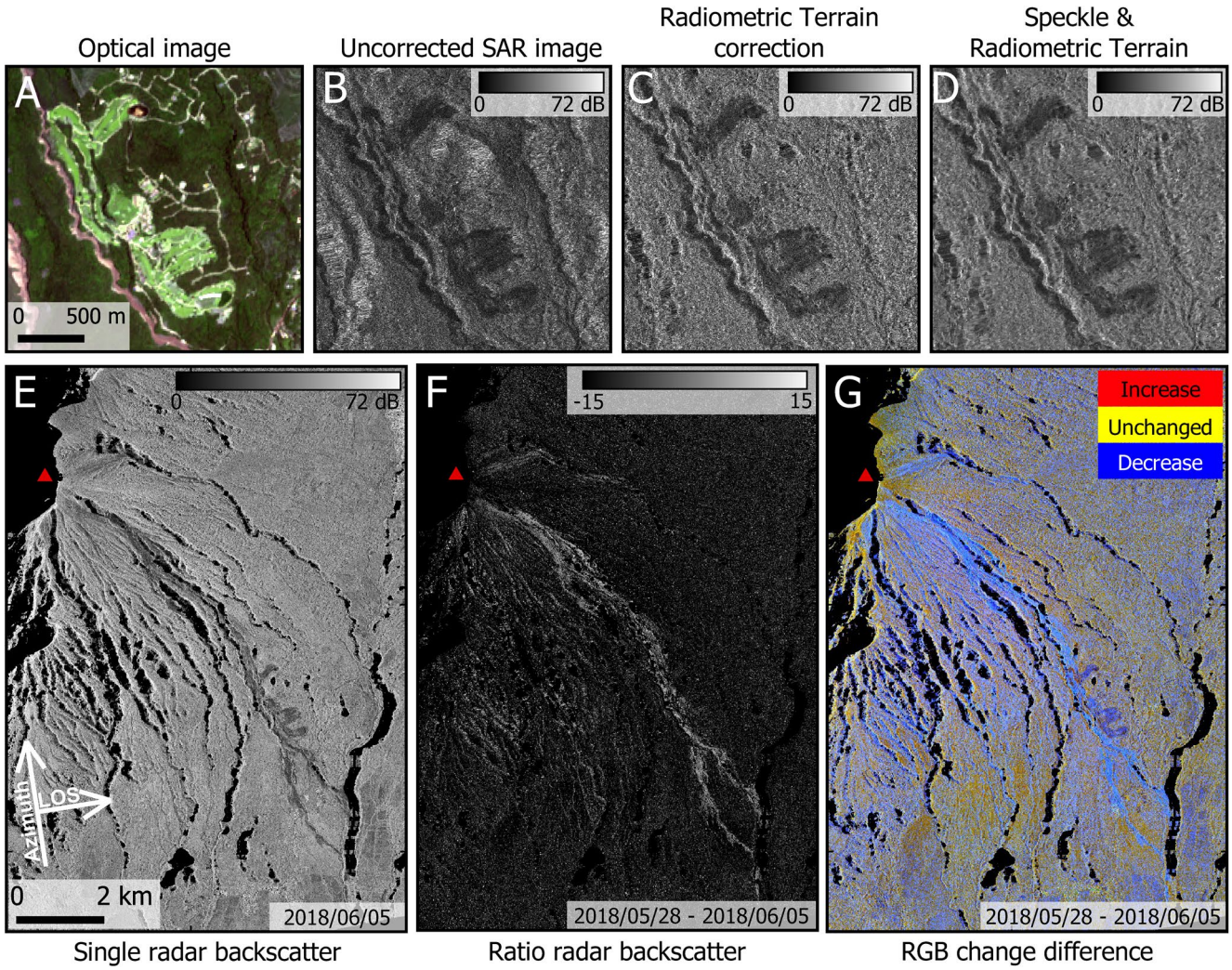

Figure 2. Corrections (b–d) and methods (e–g) applied to the backscatter dataset. La Réunion golf course in (a) Sentinel-2 optical imagery (April 20, 2018), (b–d) ascending CSK image showing the same area (b) uncorrected, (c) with a radiometric terrain correction, and (d) radiometric terrain correction and a 5 × 5 pixel Gamma-*MAP* speckle correction. (e) Single backscatter image showing the June 3, 2018 eruption; (f) ratio to emphasis areas where the backscatter changed between acquisitions; (g) RGB change difference images of pre-eruption (blue band), post-eruption (red band) and ratio (green band). Backscatter increases appear magenta and are mostly associated with the ground becoming rougher due to the emplacement of the PDCs. Backscatter decreases are cyan and are largely associated with smoothing between acquisitions. Areas that do not change between acquisitions appear yellow. Location of the scene is shown in Figure 1c.

Speckle, the constructive and destructive interference from individual scatters within a pixel, causes backscatter changes even in pixels that would otherwise remain stable between acquisitions. Speckle in SAR images can obscure signals in backscatter and complicate the data interpretation. We applied a 5 × 5 pixel adaptive Gamma-*MAP* filter, which reduces speckle while attempting to preserve structural and textural features in the radar data (Lopes et al., 1993). We found that this filter preserved the sharp boundaries of the fresh PDC deposits and man-made structures (e.g., golf course, Figure 2d) whilst reducing the speckle allowing for better comparison between acquisitions.

3. Backscatter Analysis of the June 2018 Fuego Eruption

3.1. Change Difference Backscatter Analysis

The RGB images show PDCs that descended Barranca Las Lajas during the June 3, 2018 eruption causing an overall decrease (~7 dB) in backscatter (Figure 3). There is a broad zone of backscatter change near the

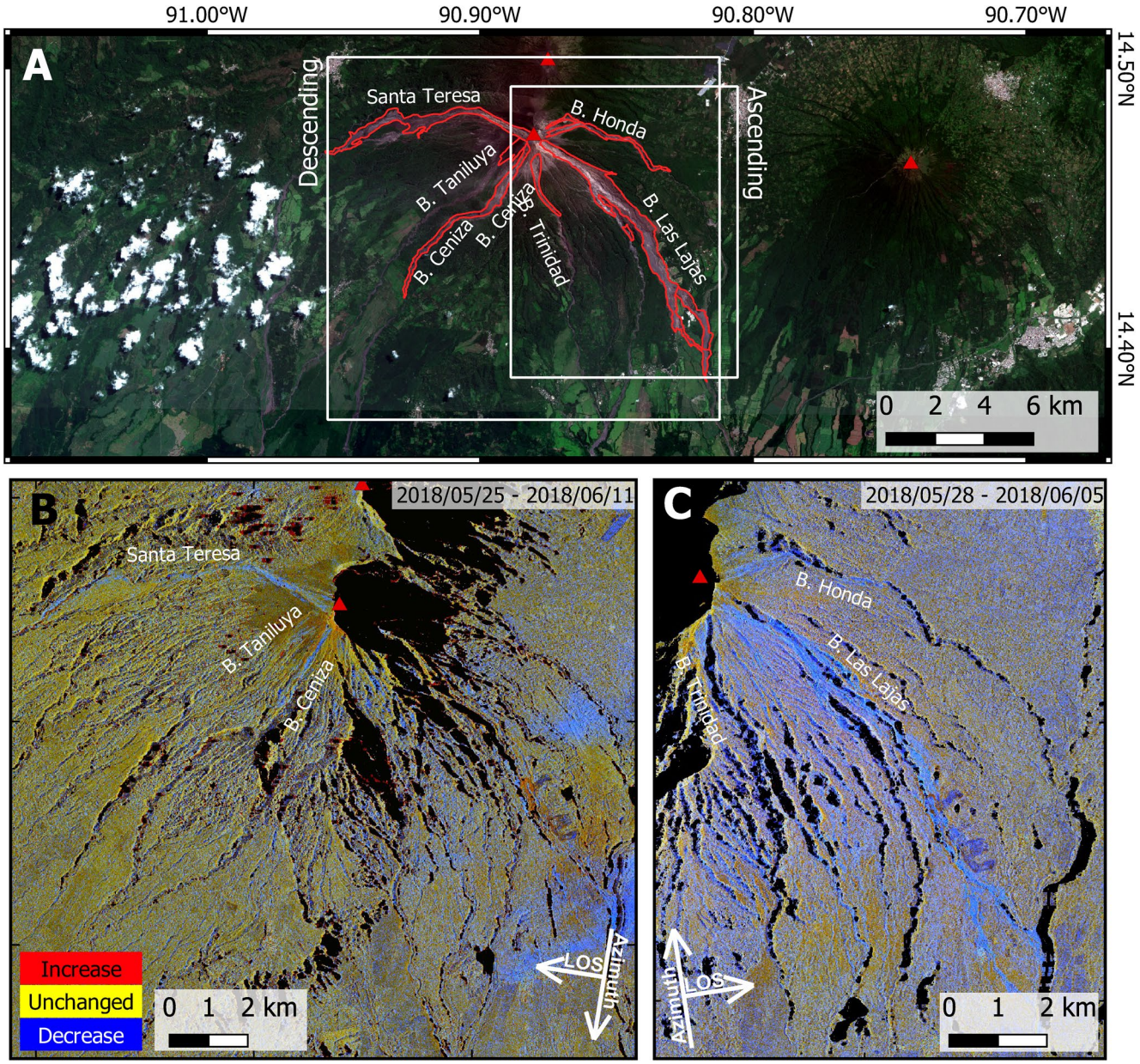

Figure 3. (a) Map of the main drainage systems on Fuego affected by the June 3, 2018 eruption, as seen by RGB change difference image using (b) ascending and (c) descending track showing backscatter changes in Barranca Honda and Barranca Las Lajas on the east flank and Barranca Santa Teresa, Barranca Taniluya and Barranca Ceniza on the west flank. Location of the scene is shown in Figure 1c.

summit, which narrows as flows are funneled into drainage channels. The deposit reduces the backscatter (blue, Figure 4a) making the ground smoother on the scale of the X-band radar wavelength (i.e., CSK, 3.1 cm). However, in the middle of the PDC path in Barranca Las Lajas there is a 60-m wide channel-like feature where backscatter increases (~1.5 dB; red, Figure 4a). The increase in backscatter roughly corresponds with lower sections of the collapse and transitional facies described in Albino et al. (2020). Where the flow overtopped (i.e., overbank, Gertisser et al., 2012) the drainage channel, the changes in backscatter depend strongly on the scattering properties of the previous surface cover resulting in complex change patterns in the lower drainage systems (e.g., dense vegetation or bare rock, Figure 4). Where a PDC removes vegetation the ground becomes smoother and the contribution of volumetric scattering is removed, resulting in a decrease in backscatter (e.g., forested area south of Barranca Santa Teresa, Figure 4b). Backscatter

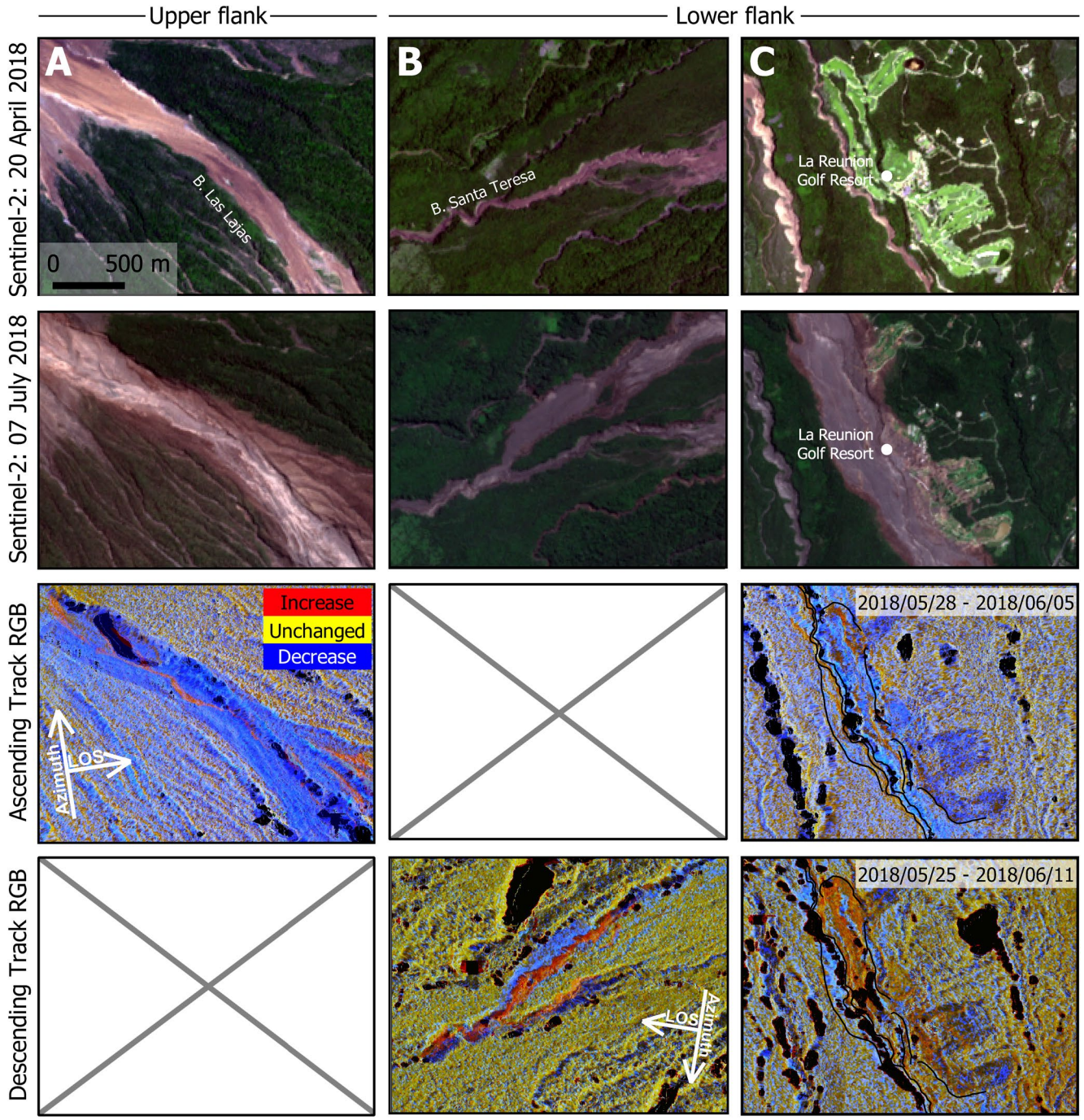

Figure 4. Backscatter changes associated with the June 3, 2018 eruption in different sections of the drainage systems. Pre- and post-eruption optical imagery and ascending CSK RGB image of (a) eastern summit area affected by PDCs in Barranca Las Lajas and (b) the lower section of Barranca Santa Teresa showing the June 3 PDCs infill and overtop (overbank) the drainage system. Blue and red overlays indicate the increases and decreases in backscatter observed from the RGB images. (c) Pre- and post-eruptive optical imagery, descending and ascending CSK RGB images over the La Réunion golf course and Barranca Las Lajas showing backscatter changes correlated with different satellite look direction and incidence angle. Areas not covered by corresponding SAR image are indicated by a gray cross. Location of the scene is shown in Figure 1c.

change patterns differ for ascending and descending CSK tracks where the PDCs interacted with vegetation or buildings (e.g., La Réunion golf course, Figure 4c), because scattering properties vary depending on the angle from which an object is viewed.

3.2. Multiple Image Backscatter Analysis

Changes in backscatter images between two dates can be noisy, and impacted by non-volcanic effects such as changes in moisture levels. We consider background noise present in backscatter images to include variations introduced by speckle, which has no temporal or spatial structure; instrument noise, which may have temporal structure, and changes to the ground surface unrelated to the volcanic eruption (e.g., moisture level), which can be spatially and temporally correlated. Using our temporally dense data set we can solve for the step associated with changes in backscatter that occur on a particular date, placing no constraint on whether the step should be positive or negative. Using a pixel-by-pixel least squares inversion (Figure 5a), we found that at least four images were required to see an improvement in the sharpness of flow edges when comparing to the ratio between two backscatter images. This method allowed for better identification of flow boundaries (Figures 5c and 5d), and lower magnitude changes that were not visible in RGB ratio images (Figure 6c). The variance of backscatter change was reduced by 31% when using a total of four rather than two images, and the addition of more dates reduced the variance even further to 42% for 15 images.

To refine our map of the June 3, 2018 eruption deposits, we make a step estimate using 14 backscatter images before the eruption and one after to avoid inclusion of later flows, slope movements and erosion present in other post-eruption acquisitions. We observe broad, low magnitude spatially correlated backscatter increases (~1.5 dB) and decreases (~3.2 dB) on the southern flank of Fuego associated with the June 3, 2018 and not apparent at any point before the eruption (e.g., same area Figures 6a and 6b have ~0.43 and ~ 0.63 dB). The difference in backscatter values for the explosive deposits are of similar orders of magnitude (e.g., ~−3.2 and ~1.5 dB, ash deposits, Figure 6g) to the background changes (~−1.3 dB, area not affected by eruption). However, the spatial structure of the backscatter changes related to new volcanic deposits are distinct from the background noise, which is dominated by spatially uncorrelated noise introduced by speckle

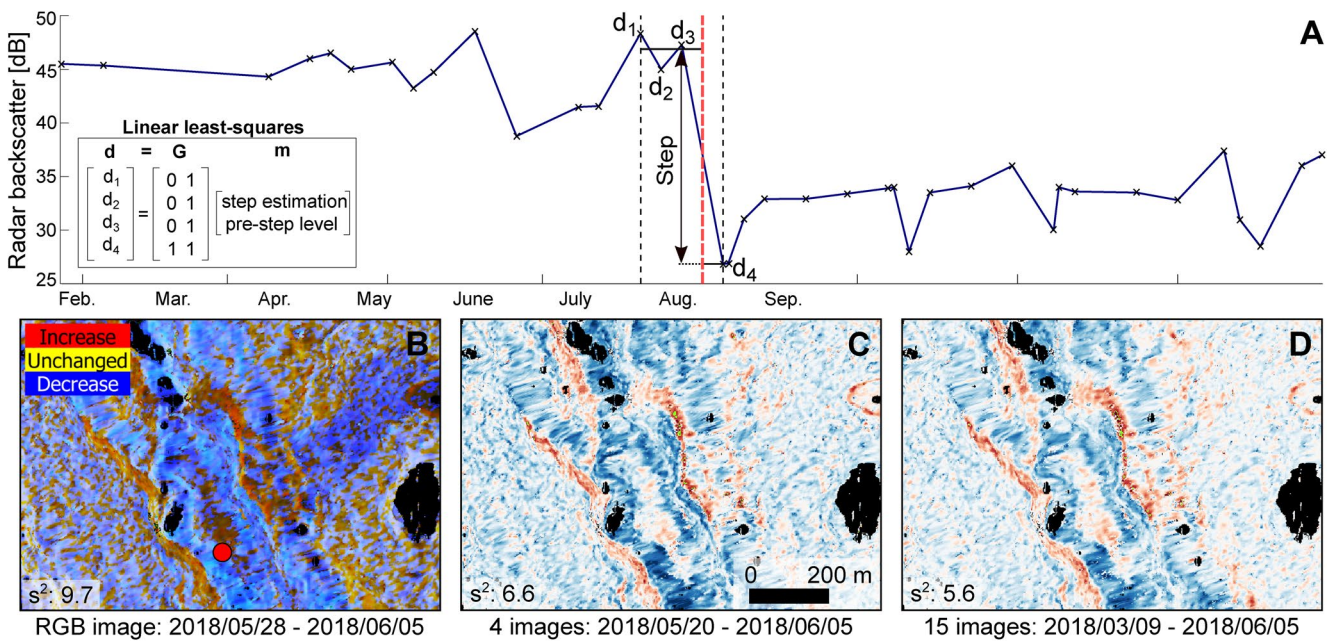

Figure 5. (a) Time series of single pixel (red dot in b) spanning the June 3, 2018 eruption (red dashed line) showing an acquisition time range (black dashed line) containing four images and the backscatter step calculated using the equation shown where "d" is the backscatter values and "G" is the design matrix. The zoomed-in images over a section of June 3, 2018 PDC deposits in Barranca Las Lajas show the changes in backscatter between 28 May 2018 and 05 June 2018 as (b) a RGB change difference image, (c)–(d) a 4- and 15-image step estimation, with variance (s^2) of background labeled. Location of the scenes is shown in Figure 1c.

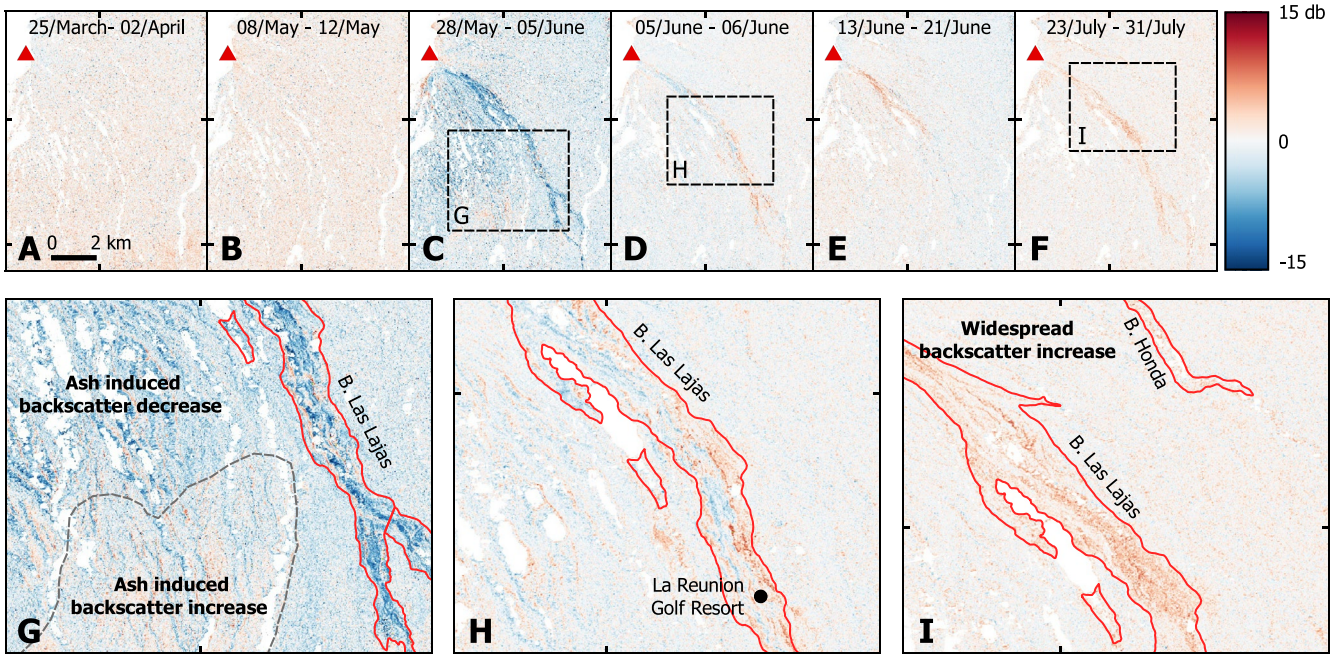

Figure 6. Step estimation (locations shown in Figure 1c) each using four acquisition dates spanning 12–24 days in total showing (a and b) backscatter variations prior to June 3, 2018 eruption, (c) the emplacement of the 3 June 2018 PDCs and ash deposits and (d and f) post-eruption emplacement of new deposits, alteration and interaction of rainfall with PDC deposits (g) and (i) detailed sections of backscatter alteration seen post-eruption.

and instrument noise. This broad change in backscatter is only observable in the first acquisition following the eruption, with backscatter changes returning to similar levels as those observed during the pre-eruption period (e.g., −1.4, 2.1 and 0.39 dB for Figures 6d–6f). Along with the limited extent and interaction with the underlying land cover, we consider this change to be associated with a major ash fallout rather than changes in backscatter caused by rainfall. We therefore attribute it to ash emplaced on 3 June 2018 that was rapidly removed during the first rainfall event that occurred on the June 5. Over densely vegetated areas of the flank the ash causes a decrease in backscatter whereas on agricultural land there is an increase (Figure 6g). Reports of ash associated with the June 3, 2018 eruption suggest ash was deposited in almost every direction for about six days, with fine ash deposits extending as far as 40 km toward the northeast (INSIVUMEH, 2018c). However, backscatter signals appear to be more limited possibly due to variations in ash thickness, ash and ground moisture content and pre-eruption land cover.

3.3. Identification of Explosive Deposits

3.3.1. Flow Deposit Mapping

The area of a flow deposit can be manually extracted from the backscatter changes but such extraction can be subjective. Solikhin et al. (2015) demonstrated the application of supervised classification techniques on L-band ALOS-PALSAR data at Merapi. This method successfully classified the different volcanic and non-volcanic deposits for dual-polarised SAR and required prior knowledge of the different deposit types and land cover present. We consider an unsupervised classification (Lu & Weng, 2007) that does not require prior knowledge or training datasets and can be applied rapidly. To keep the extraction as simple as possible we use image segmentation methods (Lu & Weng, 2007) to limit the number of subjective decisions during the extraction. We employ a morphological reconstruction (MR) on our step estimations prior to thresholding the output to extract large changes in backscatter associated with the emplacement of flow deposits (Figure 7b). MR uses a marker image that is based on the backscatter values and is able to preserve edges whilst reducing noise (e.g., Lei et al., 2018). We use a structuring element, 10–20 pixels in order to selectively reconstruct features with the characteristic spatial scale and pattern of the deposits. Following the MR, we apply a backscatter threshold (1.5–3 db for the June 3 flows), a cluster size threshold (removing groups <

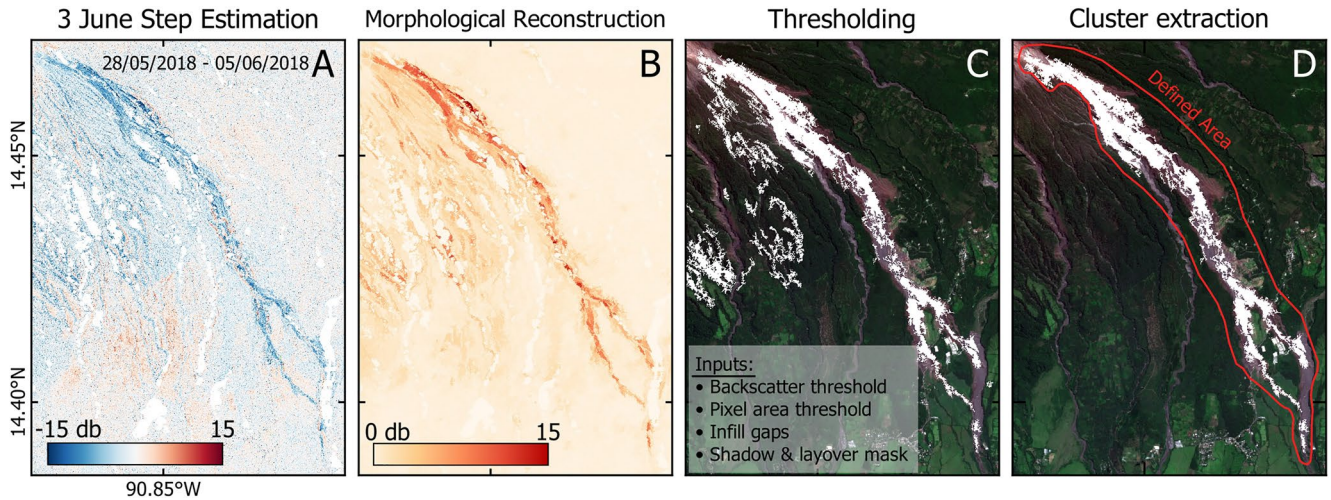

Figure 7. Semi-automatic method used to extract flow areas and lengths from (a) a 4-month step estimation using 15 CSK SAR acquisitions from February 5 to June 5, 2018 to extract the June 3, 2018 PDC in Barranca Las Lajas. (b) Morphological Reconstruction (MR) applied to step estimation image, then using (c) multiple thresholds to clear up clusters before (d) selection of clusters associated with specific flows based on drainage location and cluster pattern after thresholds. Location of the scene is shown in Figure 1c.

7,000 m^2) and fill in any small, closed gaps within the flow using a gap size threshold (Figure 7c).We aim to retain larger complete gaps because these could reflect real flow path structures. Lastly, based on the spatial pattern of clusters and, where available, information about the volcano drainage system, we select and remove large pixel clusters that are not associated with a specific deposit (e.g., signals from the ash fallout) and group clusters together depending on the deposit type (Figure 7d).

We used this semi-automatic approach to estimate the areas altered by PDCs during the June 3 eruption (Table 2). Areas extracted semi-automatically from backscatter imagery were 40–90% lower than those found manually (Table 2), with the biggest differences for smaller flows (e.g., Barranca Taniluya) where the backscatter signals are more difficult to differentiate from the surrounding noise (Figure S4). Estimates from the semi-automatic method are minima as it was not able to capture (a) low magnitude backscatter changes that were only slightly larger than background variations, (b) areas where backscatter changes from different deposits overlap or (c) areas where the flows are relatively narrow. Areas estimated from optical imagery were also consistently larger than those from the SAR imagery, perhaps because very thin deposits (e.g., Barranca Taniluya surge deposits) may have a minimal impact on backscatter values for some types of land cover.

Table 2
Lengths and Area Measurements of Fuego Drainage Systems (Location Figure 1a) Affected by the June 3, 2018 Explosive Deposits Extracted Manually and Semi-Automatically From the Step Estimation Backscatter and From Optical Imagery (Sentinel-2, July 04, 2018)

	Honda	Las Lajas	Ceniza	Taniluya	Seca	Trinidad
SAR Deposit Length (km)	6.4	11.9	8.3	1.8	9.1	> 2.5
[a]Length (km)	–	11.7	8.5	–	9.0	–
SAR area, Manual (km^2)	1.2	6.3	1.7	0.5	2.9	> 0.6
SAR areas, Semi-automatic (km^2)	0.4	4.0	0.2	–	1.1	–
SAR Percentage decrease (%)	83.3	39.7	88.2	–	62.1	–
Optical area, Manual (km^2)	1.4	7.4	1.8	1.2	3.7	1.2

[a]Measurements cited from Escobar Wolf and Ferres (2018).

3.3.2. Exploiting Full Backscatter Time Series

Backscatter changes during an eruption may be subtle, complicated by multiple events (e.g., lahar flows) or develop slowly over an extended period of time (e.g., erosional processes). To examine these types of signals, we calculate the changes in backscatter for a particular area for all possible date combinations in our dataset, producing backscatter change grids (Figure 8). These highlight temporal structures allowed us to distinguish between long-term processes (e.g., erosion and compaction) and abrupt changes that correlate to specific volcanic events (e.g., lahars).

Prior to the June 3, 2018 eruption, backscatter variations were minimal for all parts of Barranca Las Lajas (Figures 8d–8h). The 3 June PDCs caused high magnitude changes that were strongly dependent on pre-existing scattering properties (e.g., compare the valley and the golf course in Figures 8d and 8f). Backscatter changes on fresh PDC deposits between pairs of images after the 3 June 2018 eruption show more complexity, and highlight structures not easily recognizable in the individual backscatter change difference images (e.g., Figure 6). To distinguish between gradual erosion and re-working by lahars, we compare backscatter change grid patterns to rainfall data from the El Platana rain gauge (Figures 1c and 1578 m a.s.l.; 14.56°N, 90.94°W). We found that changes in backscatter (e.g., sudden changes or changes in trends) in the backscatter change grids coincided with periods of high rainfall and matched periods of reported lahars from the INSIVUMEH bulletins.

The lack of rainfall during July at Fuego (Figure 8c) allowed material to compact and resulted in gradual decrease in backscatter (June 29 and July 23, arrows in Figures 8d–8g). The next major rainfall after these drying periods are marked both by abrupt changes in backscatter in the drainage channels and by scene-wide increases in backscatter (Figures 6f and 6i) with higher magnitudes in both the newly deposited volcanic material and the agricultural land toward the south and southeast of Fuego. When the subsurface goes from dry to wet, radar penetration into the ground decreases and there is less interaction with deeper scatterers, increasing the influence of the near-surface scatterers and returning more radiation toward the satellite. We speculate that backscatter change is of higher magnitude over the looser fresh volcanic material and agricultural fields because these hold moisture better than the surrounding vegetation.

3.4. Phase Coherence of Flow Deposits

Interferometric phase coherence is very sensitive to changes in surface properties due to volcanic deposits (e.g., Dietterich et al., 2012; Wadge et al., 2002). A pixel's phase comprises contributions from all the individual scatterers within it, and its phase coherence can be estimated from the correlation between phases for a group of pixels. Exposed bed rock, roads, or any stable structure will result in high coherence values, whereas features that change between acquisitions, such as vegetation or rockfall, will cause low coherence. Both the time span between acquisitions and satellite perpendicular baseline may be proportional to the degree of phase decorrelation.

We estimate coherence by assessing the correlation of 3×3 grids of pixels for selected areas along the June 3, 2018 PDC deposits in Barranca Las Lajas for all possible image pairs to examine variations in coherence within the dataset (Figure 9). The large perpendicular baseline range of CSK images, average of 690 m between acquisitions, results in very high geometric decorrelation and many images that become entirely incoherent. By plotting the perpendicular baseline against the average coherence we identify a perpendicular baseline threshold of >700 m at Fuego, beyond which we lose all coherence except where the temporal baseline is especially low (e.g., one day interferograms).

Coherence over Fuego is very low with only ~7% of the 100 km^2 around Barranca Las Lajas and Honda showing a coherence over 0.5, even for perpendicular baseline <700 m. High coherence is limited to towns and some agricultural fields (Figure 9c), while dense vegetation and steep slopes lead to low coherence on the volcano. Prior to the June eruption, the drainage systems on the volcano flanks showed higher coherence but the emplacement of the PDCs on June 3, 2018 resulted in a sudden loss of coherence (Figure 9). In Barranca Las Lajas, the complete loss of coherence lasted for approximately a month before higher coherence values reappear. These higher coherence values in July 2018 correspond to the break in the rainy season and temporary pause in lahar activity (Figure 10a). Post-July the coherence drops slightly as the increased num-

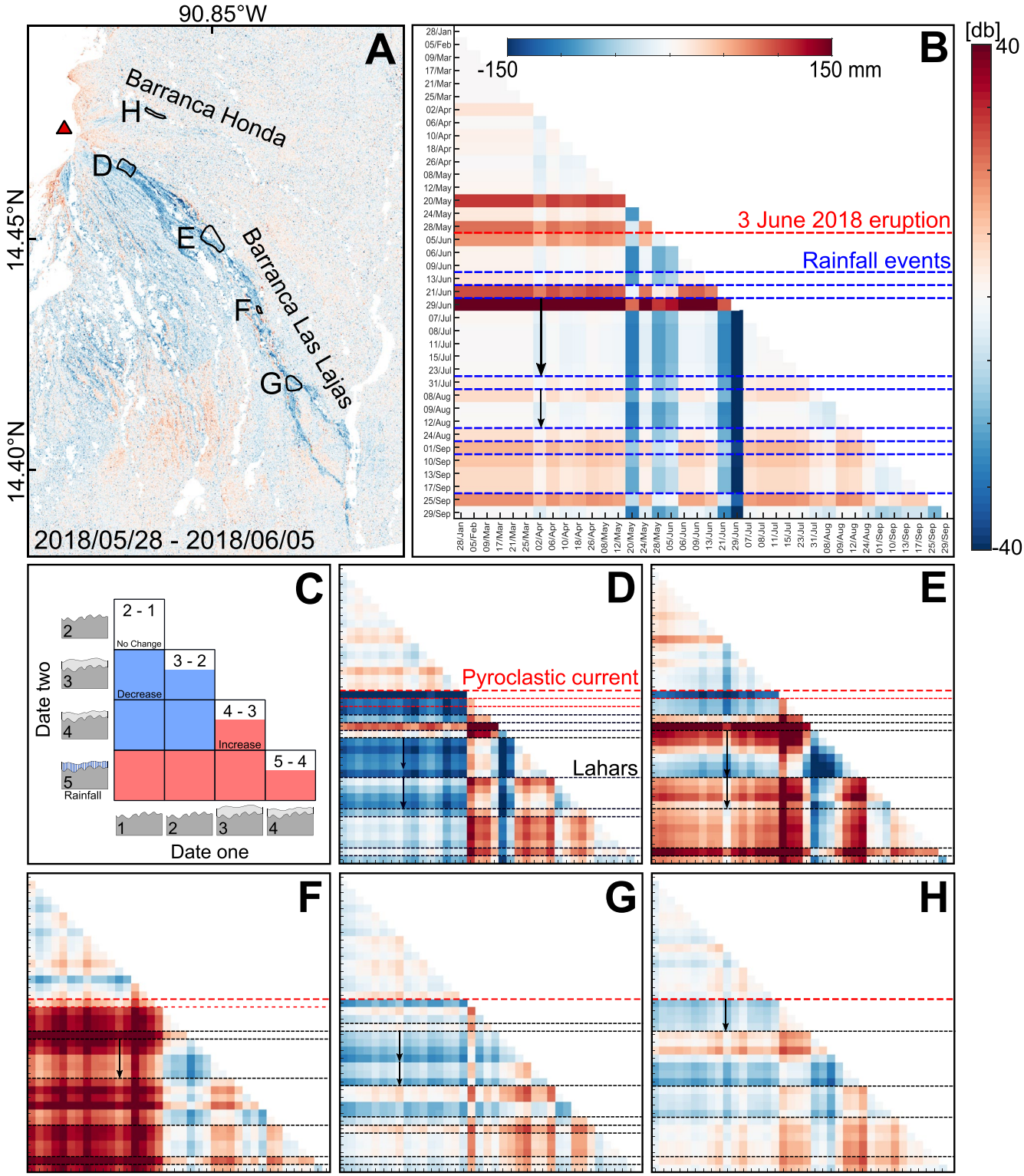
90.85°W
14.45°N
14.40°N
A
Barranca Honda
H
D
E
Barranca Las Lajas
F
G
2018/05/28 - 2018/06/05
B
-150
150 mm
3 June 2018 eruption
Rainfall events
[db]
40
-40
C
Date two
Date one
2 - 1
No Change
3 - 2
Decrease
4 - 3
Increase
5 - 4
Rainfall
D
Pyroclastic current
Lahars
E
F
G
H

Figure 8.

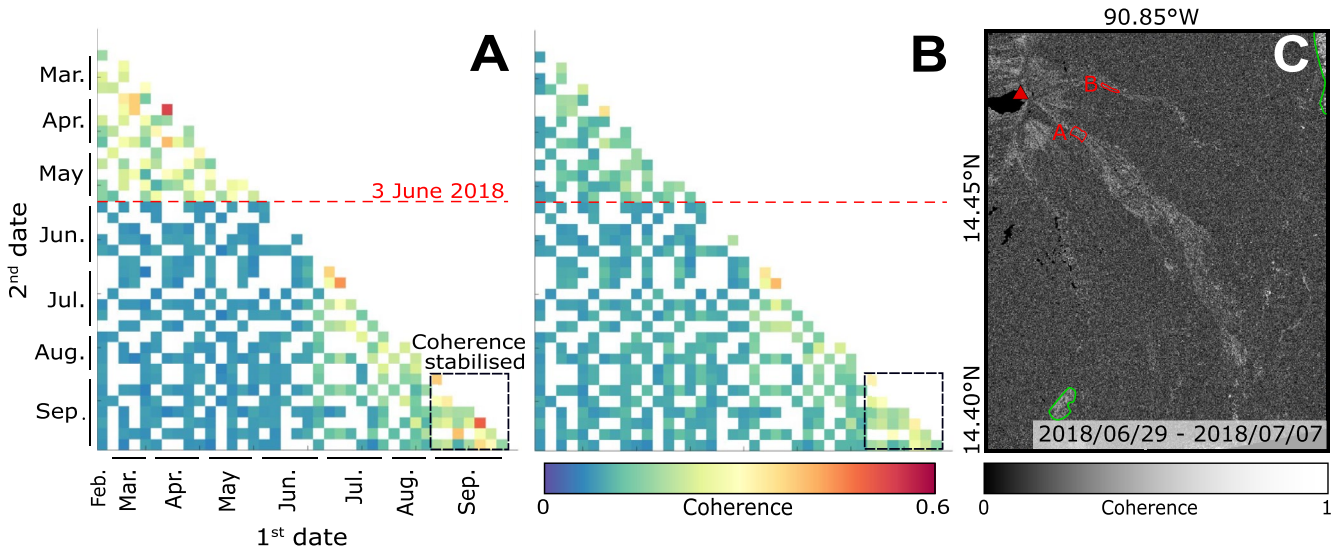

Figure 9. Radar coherence matrix for the upper sections in (a) Barranca Las Lajas and (b) Honda for areas shown in red in (c) coherence image (D and H, Figure 8a) showing the complete loss of coherence associated with the June 3, 2018 PDC, the short-term reappearance at the end of June and the return to pre-eruption coherence levels by September 2018. Coherence matrix represent the same temporal scale with white squares representing perpendicular baselines > 700 m. High coherence that correlates to towns and agricultural fields outlined in green.

ber of lahars slowly reworked the PDC material in Barranca Las Lajas. The scattering properties gradually stabilize during September 2018 and return to the pre-eruption coherence levels. Similar trends are visible in Barranca Honda (Figure 9b) demonstrating the strong correlation between lahar activity, rainfall and coherence levels. However, due to the smaller drainage and lower volcanic volume emplaced in Barranca Honda the baseline coherence is lower in the barranca reducing the magnitude of the coherence changes.

4. Discussion

4.1. June 3, 2018 Explosive Deposits

Six drainage systems at Fuego showed changes in backscatter as the result of the emplacement of PDC deposits on June 3, 2018 (Figure 3), as described in the INSIVUMEH special bulletins (INSIVUMEH, 2018d). These newly emplaced PDCs follow the pre-existing drainage down the flanks of the volcano (Figure 3). Our measurements show that the multiple flows in Barranca Las Lajas extend up to 11.9 km from the summit, altering a total area of 6.3 km^2 (Table 2) with flow thicknesses of up to 10.5 ± 2 m (Figure S2) in the lower sections of the drainage where the flow accumulated against a topographic high. Given the complexity of the topographic changes caused by the emplacement of the June 3 PDCs (Albino et al., 2020), we do not consider this sufficient to make an estimate of flow volume. Our thickness estimate compares well with topographic increases of 12 m derived from TanDEM-X data (Albino et al., 2020) for the lower portions of Barranca Las Lajas. Overall, flow lengths measured from the backscatter (Table 2) were within 0.2 km of ground-based measurements (Escobar Wolf & Ferres, 2018). Near the summit the flows channeled into different drainage systems reduced the surface roughness. The narrow band of backscatter increase we observe in Barranca Las Lajas (Figure 4a) is likely to be caused by local increases in cm-scale roughness associated with a central

Figure 8. Backscatter change grid to show long term patterns in dataset. (a) shows the locations of each backscatter change grid (Location of the scene is shown in Figure 1c). (b) Rainfall data (ICC, 2021) shown as a grid from rain gauge located 11 km northwest of Fuego, location indicated on Figure 1a. (c) Schematic showing a simplified example of how a backscatter change grid is constructed. Each square represents the difference in backscatter produced from the two ground surface cartoons. The whole grid represents all possible pair combinations in the dataset. (d–h) backscatter change grids for areas along the length of Barranca Las Lajas, Barranca Honda drainage system and in overbank deposits showing variations in backscatter patterns associated with different deposit types and location. Red line indicates June 3, 2018 eruption and PDCs, black line shows changes in backscatter attributed to lahar activity and blue line show changes attributed to rainfall.

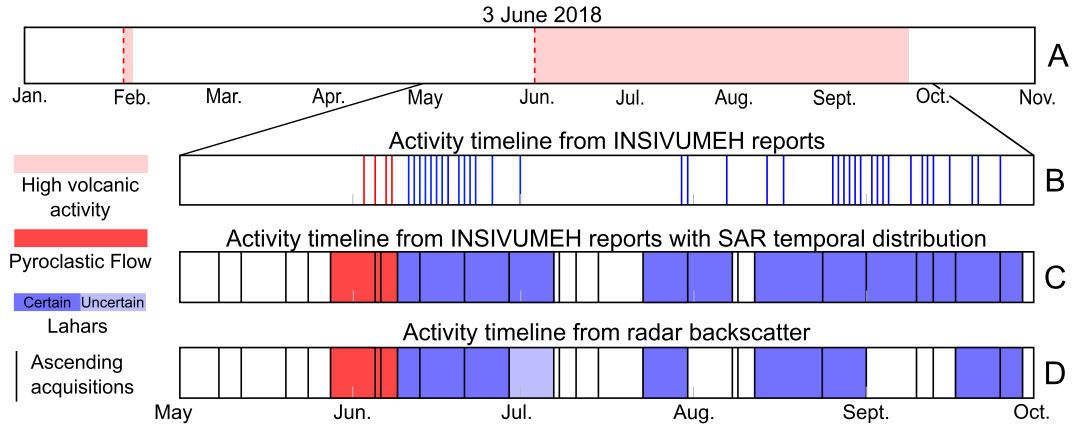

Figure 10. Timelines showing the various activity in Barranca Las Lajas. (a) shows the periods of volcanic activity in 2018 at Fuego, (b) the daily processes in Barranca Las Lajas as reported by INSIVUMEH, (c) the activity reported from the INSIVUMEH bulletins shown in the same time steps as the SAR acquisition, and (d) the timeline of volcanic activity derived from backscatter.

higher energy flow, transporting a wider range of material than in the surrounding channel. These localized increases in backscatter near the summit correlate roughly with the collapse and transitional facies described in Albino et al. (2020), where material was dominantly removed. Although changes in local slope caused by the incision of a small higher energy inner channel could also cause bands of backscatter increase, there is no indication of a new channel in the post-eruption backscatter image (June 05, 2018). Further down the drainage system, deposits were generally bounded by the channel wall and the backscatter changes are associated with different stages of valley infill and in some areas flow overbanks (Figure 4b). An approximately 40 km^2 wide area on the southern flank of Fuego showed subtle changes in backscatter that we attribute to ashfall from the initial June 3, 2018 eruption (Figures 6c and 6g). These changes are apparent only in the co-eruptive step estimation images (Section 3.2), which reduced the background backscatter noise. We attribute the backscatter decrease on the dense vegetation to the emplacement of a layer of ash, rather than the removal of leaves from vegetation, since this would produce long-term changes in backscatter that we do not observe. The impact of this ash layer on the backscatter images was short-lived and completely disappears from all other post-eruption images, which were acquired after the first major post-eruption rainfall.

Following the 3 June 2018 eruption, the backscatter remained low within Barranca Las Lajas (Figures 6d, 6h, 8d and 8e). This low backscatter was concentrated to the upper slopes of Barranca Las Lajas, extending downslope within a defined channel (Figure 6h) affected by the 3 June flow deposits. This backscatter pattern coincides with two smaller PDCs observed by INSIVUMEH on the June 5, 2018 (INSIVUMEH, 2018a, 2018g). During June and then between August to September, Fuego had periods of high lahar activity (Figure 10), which appeared as both increases and decreases in our backscatter change grid depending on the conditions and location of the lahar. We used the INSIVUMEH reports to ground truth our identification of lahar activity, and found good agreement between backscatter and field observations. From June to –September 2018, we identified nine possible periods of lahar activity in Barranca Las Lajas from backscatter alone, two of which produced small, spatially discontinuous changes or do not correlate with a major rainfall event. A period that we flagged as lahar activity with high uncertainty in June and July in Barranca Las Lajas was confirmed by in-situ observations recorded in INSIVUMEH reports (e.g., INSIVUMEH, 2018h). However, there were three periods with lahars reported by INSIVUMEH in September that are not clear from our backscatter analysis. This could be because to the flow deposits were more channeled and of smaller volume. It is also possible that their erosional and depositional impact on the backscatter was minimal.

4.2. Identification of Volcanic Products From Backscatter

Here, we discuss the approaches that were most successful for studying explosive volcanic deposits at Fuego, including the potential for automatic extraction of flow shapes.

4.2.1. Mitigating Sources of Noise

Backscatter changes caused by the emplacement of fresh explosive volcanic products may be low magnitude, small in spatial extent and differ according to scattering properties of the pre-existing land cover and topography. Interpreting backscatter therefore requires some knowledge of both pre-event scattering properties (e.g., inferred from radar, optical, or ground-based imagery) and pre-existing topography (from a global, or preferably local, DEM). Maximizing signal-to-noise ratio is also critical, and can be achieved by mitigation of noise in the backscatter.

Applying a radiometric terrain correction to the Fuego dataset reduced distortions from the steep topography allowing us to make backscatter change measurements on the steeper slopes near Fuego's summit. The high-resolution TanDEM-X-derived DEMs (10 m, September 18, 2015 and August 9, 2018) were better able to correct distortions than SRTM (30 m, February 11, 2000; Figure S2). Using both a pre- and post-eruption DEM for our analysis also minimized errors associated with differences between topography at the time of each SAR image and the DEM used for correction (especially the local gradient and location of drainage channels Figure S3). Even with a radiometric terrain correction, major differences in the satellite geometry still affect the backscatter change if the scattering mechanisms vary with incidence angle. For example, trees produce very different scattering signals depending on whether radar encounters the crown or the trunk first. This effect may account for some of the different magnitude and signs in backscatter change pattern that we observe between different tracks with different incidence angles in some locations (Figure 4c). Without the application of an adaptive filter, speckle can mask shapes and structures of the explosive volcanic deposits (Figure 2d). The adaptive Gamma-*MAP* filter (Lopes et al., 1993) improved our analysis of the backscatter changes for all methods. In our step estimation images the speckle filter made the transition between flow and surrounding areas sharper, reducing the background variance by 7% and making the subtle changes in backscatter, such as ash (Figures 6c and 6g), more easily distinguishable. For major changes such as those caused by the eruptions on 3 June, the single backscatter and change difference RGB images are sufficient to identify the main deposits. However, solving for a step in backscatter using longer time series (>30 days) and more images improved both our mapping of flow boundaries, and allowed identification of more subtle changes in backscatter (e.g., ash fall).

4.2.2. Identification of Explosive Deposits in Backscatter

In general, the significant changes to backscatter due to PDCs are limited to drainage channels and surroundings, with the sign of backscatter change dependent on radar wavelength, flow roughness and pre-eruption scattering properties. It may take the backscatter a few days, months, or years to return to pre-eruption levels of backscatter (e.g., for vegetation to grow back where it was completely removed). However, backscatter can also remain permanently altered and never return to the values it had before the eruption (e.g., complete restructure of drainages systems).

Backscatter signatures of major PDCs have been identified at Soufrière Hills Volcano, Montserrat using TerraSAR-X (X-band; Wadge et al., 2011) and the 2010 Merapi eruption with ALOS-PALSAR (L-band; Solikhin et al., 2015). For Fuego (Figure 4) and Soufrière Hills Volcano, pyroclastic surge deposits were associated with decreases in backscatter. However, pyroclastic surge deposits at Merapi caused an increase in the backscatter. There are also similarities in backscatter patterns within flows at different eruptions. At Fuego and Soufrière Hills Volcano, narrow bands of increased backscatter occur in the middle of PDC deposits, inside the main channels (e.g., Figure 4a), which we attribute to fresh block and ash deposits, including larger, up to meter-scale blocks that dominate the backscatter signal. However, for the 2010 Merapi eruption, a narrow band of decreased backscatter was observed in the center of the flow where the most energetic flows were deposited. The differences between observations at Merapi, Fuego and Montserrat are consistent with the different roughness lengths scales to which L-band ($\lambda = 23$ cm) and X-band ($\lambda = 3.1$ cm) radar are sensitive. The Rayleigh Criterion, $h > \frac{\lambda}{8cos(\theta)}$, provides a material size threshold of whether a surface is appears 'rough' (bright) or 'smooth' (dark) in backscatter. For X-band, objects <0.4 cm appear smooth while for L-band objects <3.6 cm will appear smooth. This means that material between 0.4 and 3.6 cm will produce different backscatter signals at L- and X-band wavelengths. Lahars produce much more subtle signals in backscatter limited to active drainages and freshly deposited material. Distinguishing between the sudden changes caused by a lahar and more gradual erosion is particularly challenging using

non-continuous imagery. The addition of rainfall data provides some constraint on when lahars are more likely to have occurred. The use of dense SAR time series with short revisit times is also critical. The Fuego lahars produce both increases and decreases in backscatter at different positions along the flow path. In general, the upper sections of drainages are dominated by erosion, reducing the backscatter, while surface roughness increases downslope as larger blocks are deposited. Multiple lahars of different sizes and magnitude may occur during the several days between SAR acquisitions so that the backscatter change patterns do not represent a single lahar event. The backscatter change caused by lahars is also sensitive to the timing of rainfall; high rainfall closer to the second acquisition produces a higher magnitude change than if it were close to first acquisition and the ground had time to dry out. Although backscatter signals from lahars are superficially similar to those from gradual erosion and deposition in any image pair, we found that we could identify lahar signals at Fuego by finding turning points in backscatter sign in the time series (Figure 8) and comparing their timing to high rainfall events (Figure 8c).

The backscatter changes associated with the emplacement of ash fallout from 3 June eruption are much more widespread than either the PDCs or lahar deposits. In general, backscatter signals from ash reach their maximum close to the eruptive vent of the volcano and are characterized by short-lived changes. The sign of the change is dependent on the pre-eruption land cover, the moisture content of the ground and the ash, whether the deposit coats the ground or is thick enough to remove or destroy vegetation. Although ash deposits are spatially systematic, they may produce only very small magnitude variations in backscatter, difficult to differentiate from background noise. Therefore, reliable corrections for noise (e.g., speckle) are necessary, especially as the impact of ash on SAR backscatter (e.g., the impact of thickness variations, morphology, and dielectric properties) is poorly understood. At Fuego, we measure both an increase and decrease in backscatter caused by ashfall over different surfaces, but at Nabro (June 2011, Goitom et al., 2015) the pre-eruption land cover was a uniform semi-arid environment, resulting in a decrease in backscatter signal linked to topographic smoothing. For both Fuego and Nabro eruptions, backscatter changes related to ash were dominated by changes in the surface roughness. However, the ash at Cotapaxi, Ecuador (August 2015, Arnold et al., 2018) had a high moisture content producing an increase in backscatter and masking any decrease in surface roughness. Although ash deposition generates a clear backscatter change signal for some eruptions (e.g., Nabro, Eritrea, Goitom et al., 2015), this depends strongly on the ground's scattering properties pre-eruption, as well as deposit thickness and may be much more subtle, as seen at 2018 Fuego eruption. In these cases, longer time series are more adept at extracting these types of signals.

4.2.3. Potential for Automated Flow Shape Extraction

While our study of the 2018 Fuego eruption is retrospective, analysis of backscatter has great potential as a tool to track the progression of an eruption, especially where visual observations are limited. We assess the accuracy of the areas and lengths generated by our semi-automatic approach (Section 3.3.1) by comparing them to measurements extracted manually from backscatter (Table 2) and optical imagery (i.e., Sentinel-2, July 4, 2018, Table 2). Although Sentinel-2 is limited by low resolution (10 m) and there is a gap of 26 days after the start of the eruption before the first clear image, we found the images suitable for the comparison at Fuego and the recurring acquisition and greater number of images translated into more cloud-free pixels over time. For Barranca Las Lajas the semi-automatically identified area was ~38% smaller than through manual extraction, while flows where backscatter variations were not significantly different to the background noise (e.g., Barranca Taniluya, Figure S4) showed up to ~85% difference. Using smaller MR structuring elements and lower thresholds allowed us to extract some of these flow shapes, reducing these values too far resulted in false positives especially in areas where the surrounding variations were large (e.g., summit or ash on south flank). False positives were also associated with overlapping deposit distributions, signals from volcanic ash on the southern flank merged with changes associated to the flow in Barranca Trinidad and upper sections of Barranca Las Lajas in June 2018 (Figure 6c). Morphological operators and image segmentation limited bias in the identification of flows. However, the semi-automatic method was less effective where backscatter changes were low magnitude (e.g., Barranca Honda, Figure 3c), where changes were similar to the level of background noise, or where the boundaries showed gradual transitions (false negatives).

The flow areas measured from optical imagery (Table 2) were larger for all drainages than seen in the backscatter images. This may be because the first SAR image was acquired two days post eruption, while the first completely cloud free Sentinel-2 optical image was acquired over a month later on the July 4, 2018 and

captures multiple events, not seen in the SAR image pair. Further, some deposits (e.g., overbank deposits in lower Barranca Seca, Figure 4b) visible in the optical imagery either do not change the radar scatterers enough to cause a difference in backscatter, or different signal contributions (e.g., from roughness and moisture) cancel each other out. For example, the backscatter would show a decrease for a rough surface becoming smoother and an increase for a dry surface becoming wet. A rough, dry surface that changes to a smooth wet one may produce minimal backscatter change. A deposit that produces changes in all contributing factors: local slope, centimetre-scale roughness, and moisture, produces a very complicated change pattern, with the potential for some flow sections to produce minimal or non-observable change signals.

4.3. Application to Explosive Volcanoes Globally

The high spatial resolution and temporal density provided by CSK SAR images are ideal for analysis of explosive volcanic eruptions using backscatter. However, CSK is a commercial constellation and although it has a good volcano background mission, it is not free or open, although it is available to observatories and research scientists through programs such as the CEOS Volcano Demonstrator (Pritchard et al., 2018). We therefore present a short comparison of the backscatter methods we applied in this study to completely open-access data. We use the freely available C-band (5.6 cm) Sentinel-1 data (~5 × 20 m) and SRTM-DEM (30 m).

The June 3, 2018 Fuego eruption produced fundamentally similar signals in both CSK and Sentinel-1 data, which both captured backscatter changes in all affected drainage systems (Figure 11). The pyroclastic surge in Barranca Trinidad (not reported in the INSIVUMEH eruption reports), which is partially masked in the CSK images (Figure 3) due to the satellite geometry, is clearer in the Sentinel-1 imagery. While the Sentinel-1 change difference and step image (Figure 11) showed similar overall spatial extent for the PDC deposits, the lower resolution does not capture the finer detail seen in the CSK data (e.g., complexity around La Réunion golf course, the overbank flow at San Miguel Los Lotes ash fallout on southwest flank). The longer repeat time for S1 data results in the combination of multiple events and long term changes into a single step image. This long temporal span could cause masking or the reduction of backscatter changes associated with particular events making the identification of different individual events impossible. Nevertheless, the global availability of Sentinel-1 data allows for frequent (6–12 days) observation and interpretation of explosive volcanic eruptions.

Both high perpendicular baselines in our data set, and the tropical vegetation at Fuego meant we observed very low interferometric phase coherence. In other settings (e.g., Dietterich et al., 2012), phase coherence could provide completely independent comparison to flow extent maps derived from backscatter. However, as the 3 June eruption occurred following a few months of low volcanic activity, coherence before the June 2018 eruption was high enough in some drainage channels that we were able to detect the emplacement and post-eruption development of deposits. While L-band sensors (e.g., ALOS-2) would provide with higher overall coherence, the X-band CSK images used in this case study had the particular advantage of being a much temporally denser data set.

Backscatter changes are dependent not only on the type of explosive deposit, but on specific conditions at the volcano including underlying ground cover (e.g., vegetation) and moisture levels. Therefore, to be able to accurately interpret what backscatter changes during a particular eruption mean, a good understanding of the volcano setting (e.g., local topography, ground coverage) is needed.

5. Conclusion

We provide a thorough application of multiple backscatter methods to examine explosive volcanic deposits of the 2018 activity at Volcán de Fuego, Guatemala. We use SAR backscatter to map six drainages affected by PDCs (Table 2) during the June 3, 2018 eruption accompanied by backscatter changes associated with ashfall. The major PDC sequence in Barranca Las Lajas showed an extent of 11.9 km from the summit covering an area of 6.3 km^2 and with a thickness up to 10.5 ± 2 m in the lower section. The backscatter signals associated with the Barranca Las Lajas deposits showed increases related to the block and ash deposits within the channel and wider spread decreases in backscatter linked to the emplacement of pyroclastic surge and overbank deposits. Between June and September 2018, we observed two more PDCs in Barranca

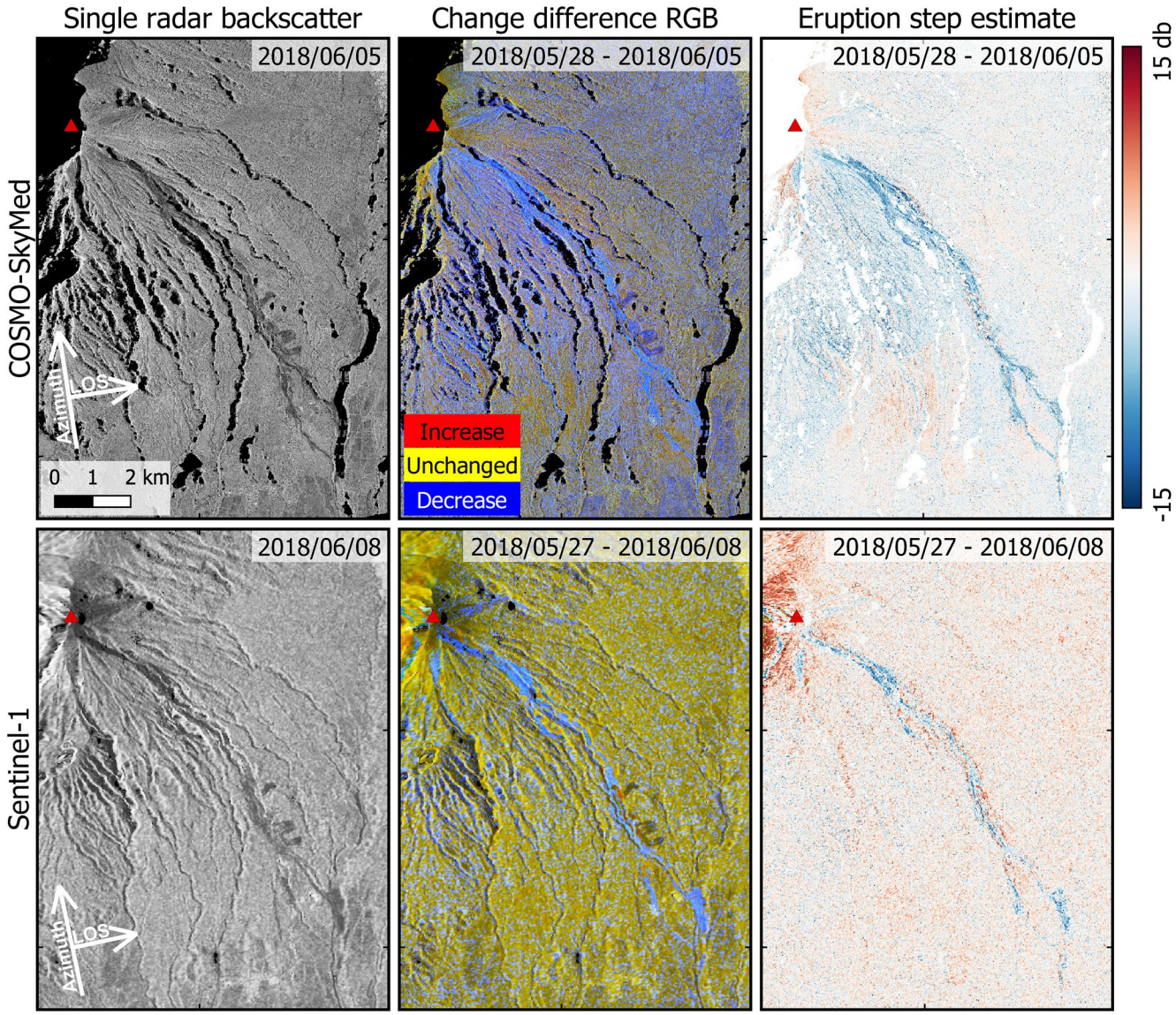

Figure 11. Comparison of Sentinel-1 and CSK backscatter methods for the 3 June 2018 PDCs in Barranca Las Lajas. A radiometric terrain correction and speckle filters were applied to both Sentinel-1 (using the SRTM 30 m DEM and a 3 × 3 pixel window) and CSK (using the TanDEM-X derived 10 m DEMs and a 5 × 5 pixel window). Location of the scene is shown in Figure 1c.

Las Lajas and, with additional information from local rainfall data and INSIVUMEH reports, nine periods of potential high lahar activity.

We demonstrate that solving for a step change in backscatter from a time series improved signal-to-noise ratio and aided the identification of explosive volcanic deposits. The use of time series backscatter change show temporal patterns that have potential to identify lahars and more gradual post-eruption erosion processes.

This work demonstrates the suitability of SAR backscatter for monitoring the progression of explosive eruptions and the subsequent alteration of their deposits. We demonstrate that not only PDCs can be mapped using backscatter, but that subsequent lahars and ash fallout can be distinguished from background noise. This case study shows the potential of the backscatter datasets to provide useful observations and measurements for volcano monitoring when optical, radar phase or ground-based observations are limited.

Data Availability Statement

Sentinel-1 imagery are freely available from ESA's Copernicus Open Access Hub and older imagery can be requested from the Long Term Archives (https://scihub.copernicus.eu/userguide/LongTermArchive).

Acknowledgments
This work was supported by the European Space Agency (ESA Living Planet Fellowship to SKE), the NERC-BGS Center for Observation and Modeling of Earthquakes, Volcanoes, and Tectonics (COMET) and the University of Leeds. SKE is supported by a NERC Independent Research Fellowship (NE/R015546/1). We acknowledge the CEOS Working Group on Disasters Volcano Demonstrator and ASI for providing 19 COSMO-SkyMed spanning January–October 2018. We thank Juliet Biggs, Matthew Watson, ASI and INSIVUMEH for coordinating the provision of 43 COSMO-SkyMed images spanning the June 2018 eruption (March–August 2018). CSK imagery, provided by ASI, can be requested through the CEOS Volcano Demonstrator Program, by contacting either the demonstrator leads or the WGDisasters secretariat (https://ceos.org/ourwork/workinggroups/disasters/). We would like to thank M. Watson and H. Wright for valuable discussion on the 2018 Fuego eruption.

References

Albino, F., Biggs, J., Escobar-Wolf, R., Naismith, A., Watson, M., Phillips, J., & Marroquin, G. C. (2020). Using TanDEM-X to measure pyroclastic flow source location, thickness and volume: Application to the 3rd June 2018 eruption of Fuego volcano, Guatemala. *Journal of Volcanology and Geothermal Research*, *406*, 107063. https://doi.org/10.1016/j.jvolgeores.2020.107063

Arnold, D. W., Biggs, J., Anderson, K., Vallejo Vargas, S., Wadge, G., Ebmeier, S. K., & Mothes, P. (2017). Decaying lava extrusion rate at El Reventador Volcano, Ecuador, measured using high-resolution satellite radar. *Journal of Geophysical Research: Solid Earth*, *122*(12), 9966–9988. https://doi.org/10.1002/2017JB014580

Arnold, D. W., Biggs, J., Wadge, G., & Mothes, P. (2018). Using satellite radar amplitude imaging for monitoring syn-eruptive changes in surface morphology at an ice-capped stratovolcano. *Remote Sensing of Environment*, *209*, 480–488. https://doi.org/10.1016/j.rse.2018.02.040

Barrière, J., d'Oreye, N., Oth, A., Geirsson, H., Mashagiro, N., Johnson, J. B., & Kervyn, F. (2018). Single-station seismo-acoustic monitoring of Nyiragongo's Lava Lake activity (DR Congo). *Frontiers in Earth Science*, *6*, 82. https://doi.org/10.3389/feart.2018.00082

Carn, S. A. (1999). Application of synthetic aperture radar (SAR) imagery to volcano mapping in the humid tropics: A case study in East Java, Indonesia. *Bulletin of Volcanology*, *61*(1–2), 92–105. https://doi.org/10.1007/s004450050265

Carr, M. J., Patino, L. C., & Feigenson, M. D. (2007). *Petrology and geochemistry of lavas*. Taylor and Francis.

Castro, J. M., Cordonnier, B., Schipper, C. I., Tuffen, H., Baumann, T. S., & Feisel, Y. (2016). Rapid laccolith intrusion driven by explosive volcanic eruption. *Nature Communications*, *7*(1), 1–7. https://doi.org/10.1038/ncomms13585

Delgado, F., Kubanek, J., Anderson, K. R., Lundgren, P., & Pritchard, M. (2019). Physicochemical models of effusive rhyolitic eruptions constrained with InSAR and DEM data: A case study of the 2011-2012 Cordon Caulle eruption. *Earth and Planetary Science Letters*, *524*, 1–14. https://doi.org/10.1016/j.epsl.2019.115736

Dietterich, H. R., Poland, M. P., Schmidt, D. A., Cashman, K. V., Sherrod, D. R., & Espinosa, A. T. (2012). Tracking lava flow emplacement on the east rift zone of Kilauea, Hawai'i, with synthetic aperture radar coherence. *Geochemistry, Geophysics, Geosystems*, *13*(5), Q05001. https://doi.org/10.1029/2011GC004016

Di Traglia, F., Nolesini, T., Ciampalini, A., Solari, L., Frodella, W., Bellotti, F., & Casagli, N. (2018). Tracking morphological changes and slope instability using spaceborne and ground-based SAR data. *Geomorphology*, *300*, 95–112. https://doi.org/10.1016/j.geomorph.2017.10.023

Dumont, S., Sigmundsson, F., Parks, M. M., Drouin, V. J. P., Pedersen, G. B. M., Jónsdóttir, I., & Oddsson, B. (2018). Integration of SAR Data Into Monitoring of the 2014–2015 Holuhraun Eruption, Iceland: Contribution of the Icelandic Volcanoes Supersite and the FutureVolc Projects. *Frontiers of Earth Science*, *6*, 231. https://doi.org/10.3389/feart.2018.00231

Ebmeier, S. K., Andrews, B. J., Araya, M. C., Arnold, D. W., Biggs, J., Cooper, C., & Williamson, J. L. (2018). Synthesis of global satellite observations of magmatic and volcanic deformation: Implications for volcano monitoring & the lateral extent of magmatic domains. *Journal of Applied Volcanology*, *7*(1), 1–26. https://doi.org/10.1186/s13617-018-0071-3

Ebmeier, S. K., Biggs, J., Muller, C., & Avard, G. (2014). Thin-skinned mass-wasting responsible for widespread deformation at Arenal volcano. *Frontiers of Earth Science*, *2*, 35. https://doi.org/10.3389/feart.2014.00035

Escobar Wolf, R., & Ferres, D. (2018). *Informe Tecnico: Volcan de Fuego Technical Report. Cooperacion Espanola*. Retrieved from http://bibliotecadigital.aecid.es/bibliodig/i18n/consulta/registro.cmd?id=8751

Flores-Anderson, A. I., Herndon, K. E., Thapa, R. B., & Cherrington, E. (2019). The SAR Handbook: Comprehensive methodologies for forest monitoring and biomass estimation. *SERVIR Global*. https://doi.org/10.25966/nr2c-s697

Fournier, T. J., Pritchard, M. E., & Riddick, S. N. (2010). Duration, magnitude, and frequency of subaerial volcano deformation events: New results from Latin America using InSAR and a global synthesis. *Geochemistry, Geophysics, Geosystems*, *11*(1). https://doi.org/10.1029/2009GC002558

Gertisser, R., Cassidy, N. J., Charbonnier, S. J., Nuzzo, L., & Preece, K. (2012). Overbank block-and-ash flow deposits and the impact of valley-derived, unconfined flows on populated areas at Merapi volcano, Java, Indonesia. *Natural Hazards*, *60*(2), 623–648. https://doi.org/10.1007/s11069-011-0044-x

Global Volcanism Program. (2005). Report on Fuego (Guatemala). In R. Wunderman (Ed.), Bulletin of the global volcanism network (Vol. 30, p. 8). Smithsonian Institution. https://doi.org/10.5479/si.GVP.BGVN200508-342090

Goitom, B., Oppenheimer, C., Hammond, J. O., Grandin, R., Barnie, T., Donovan, A., & Berhe, S. (2015). First recorded eruption of Nabro volcano, Eritrea, 2011. *Bulletin of Volcanology*, *77*(10), 85. https://doi.org/10.1007/s00445-015-0966-3

ICC. (2021). *Instituto Privado de Investigación sobre Cambio Climático (ICC): El Platanar*. [Online]. Retrieved on Novemeber 2019, from https://redmet.icc.org.gt/

INSIVUMEH. (2018a). Descenso de Flujos Piroclásticos (Vol. 36). Bolentín Vulcanólogico Especial, Volcán de Fuego.

INSIVUMEH. (2018b). Descento de Flujos Piroclásticos Hacia La Barranca Seca (Vol. 59). Bolentín Vulcanólogico Especial, Volcán de Fuego.

INSIVUMEH. (2018c). *Erupcion con Flujoc Piroclásticos* (Vol.27). Bolentín Vulcanólogico Especial, Volcán de Fuego.

INSIVUMEH. (2018d). *Finaliza la erupcion* (Vol. 33). Bolentín Vulcanólogico Especial, Volcán de Fuego.

INSIVUMEH. (2018e). Flujos Piroclásticos Barranca Las Lajas (Vol. 44). Bolentín Vulcanólogico Especial, Volcán de Fuego.

INSIVUMEH. (2018f). Flujos Piroclásticos Barranca Las Lajas (Vol. 47). Bolentín Vulcanólogico Especial, Volcán de Fuego.

INSIVUMEH. (2018g). Flujos Piroclásticos Barranca Las Lajas Y Jute (Vol. 38). Bolentín Vulcanólogico Especial, Volcán de Fuego.

INSIVUMEH. (2018h). Lahares Moderados en la Barranca: Las Lajas Y Honda (Vol. 127). Bolentín Vulcanólogico Especial, Volcán de Fuego.

Kubanek, J., Westerhaus, M., & Heck, B. (2017). TanDEM-X time series analysis reveals lava flow volume and effusion rates of the 2012-2013 Tolbachik, Kamchatka fissure eruption. *Journal of Geophysical Research: Solid Earth*, *122*(10), 7754–7774. https://doi.org/10.1002/2017jb014309

Lei, T., Jia, X., Zhang, Y., He, L., Meng, H., & Nandi, A. K. (2018). Significantly fast and robust fuzzy c-means clustering algorithm based on morphological reconstruction and membership filtering. *IEEE Transactions on Fuzzy Systems*, *26*(5), 3027–3041. https://doi.org/10.1109/tfuzz.2018.2796074

Lopes, A., Nezry, E., Touzi, R., & Laur, H. (1993). Structure detection and statistical adaptive speckle filtering in SAR images. *International Journal of Remote Sensing*, *14*(9), 1735–1758. https://doi.org/10.1080/01431169308953999

Lu, D., & Weng, Q. (2007). A survey of image classification methods and techniques for improving classification performance. *International Journal of Remote Sensing*, *28*(5), 823–870. https://doi.org/10.1080/01431160600746456

Lyons, J. J., Waite, G. P., Rose, W. I., & Chigna, G. (2010). Patterns in open vent, strombolian behavior at Fuego volcano, Guatemala, 2005-2007. *Bulletin of Volcanology*, *72*(1), 1–15. https://doi.org/10.1007/s00445-009-0305-7

Martin, D. P., & Rose, W. I. (1981). Behavioral patterns of Fuego volcano, Guatemala. *Journal of Volcanology and Geothermal Research*, *10*(1–3), 67–81. https://doi.org/10.1016/0377-0273(81)90055-X

Meyer, F. J., McAlpin, D. B., Gong, W., Ajadi, O., Arko, S., Webley, P. W., & Dehn, J. (2015). Integrating SAR and derived products into operational volcano monitoring and decision support systems. *ISPRS Journal of Photogrammetry and Remote Sensing*, *100*, 106–117. https://doi.org/10.1016/j.isprsjprs.2014.05.009

Moore, C., Wright, T., Hooper, A., & Biggs, J. (2019). The 2017 eruption of Erta 'Ale Volcano, Ethiopia: Insights into the shallow axial plumbing system of an incipient Mid-Ocean Ridge. *Geochemistry, Geophysics, Geosystems*, *20*(12), 5727–5743. https://doi.org/10.1029/2019GC008692

Naismith, A. K., Armijos, M. T., Escobar, E. A. B., Chigna, W., & Watson, I. M. (2020). Fireside tales: Understanding experiences of previous eruptions and factors influencing the decision to evacuate from activity of Volcán de Fuego. *Volcanica*, *3*(2), 205–226. https://doi.org/10.30909/vol.03.02.205226

Naismith, A. K., Watson, I. M., Escobar-Wolf, R., Chigna, G., Thomas, H., Coppola, D., & Chun, C. (2019). Eruption frequency patterns through time for the current (1999–2018) activity cycle at Volcán de Fuego derived from remote sensing data: Evidence for an accelerating cycle of explosive paroxysms and potential implications of eruptive activity. *Journal of Volcanology and Geothermal Research*, *371*, 206–219. https://doi.org/10.1016/j.jvolgeores.2019.01.001

Ozawa, T., & Kozono, T. (2013). Temporal variation of the Shinmoe-dake crater in the 2011 eruption revealed by spaceborne SAR observations. *Earth Planets and Space*, *65*(6), 527–537. https://doi.org/10.5047/eps.2013.05.004

Pallister, J. S., Schneider, D. J., Griswold, J. P., Keeler, R. H., Burton, W. C., Noyles, C., & Ratdomopurbo, A. (2013). Merapi 2010 eruption-chronology and extrusion rates monitored with satellite radar and used in eruption forecasting. *Journal of Volcanology and Geothermal Research*, *261*, 144–152. https://doi.org/10.1016/j.jvolgeores.2012.07.012

Pardini, F., Queißer, M., Naismith, A., Watson, I., Clarisse, L., & Burton, M. (2019). Initial constraints on triggering mechanisms of the eruption of Fuego volcano (Guatemala) from 3 June 2018 using IASI satellite data. *Journal of Volcanology and Geothermal Research*, *376*, 54–61. https://doi.org/10.1016/j.jvolgeores.2019.03.014

Patrick, M. R., Harris, A. J., Ripepe, M., Dehn, J., Rothery, D. A., & Calvari, S. (2007). Strombolian explosive styles and source conditions: Insights from thermal (FLIR) video. *Bulletin of Volcanology*, *69*(7), 769–784. https://doi.org/10.1007/s00445-006-0107-0

Pedersen, G. B., Höskuldsson, A., Dürig, T., Thordarson, T., Jónsdóttir, I., Riishuus, M. S., & Schmith, J. (2017). Lava field evolution and emplacement dynamics of the 2014–2015 basaltic fissure eruption at Holuhraun, Iceland. *Journal of Volcanology and Geothermal Research*, *340*, 155–169. https://doi.org/10.1016/j.jvolgeores.2017.02.027

Plank, S., Walter, T. R., Martinis, S., & Cesca, S. (2019). Growth and collapse of a littoral lava dome during the 2018/19 eruption of Kadovar Volcano, Papua New Guinea, analyzed by multi-sensor satellite imagery. *Journal of Volcanology and Geothermal Research*, *388*, 106704. https://doi.org/10.1016/j.jvolgeores.2019.106704

Pritchard, M. E., Biggs, J., Wauthier, C., Sansosti, E., Arnold, D. W., Delgado, F., & Zoffoli, S. (2018). Towards coordinated regional multi-satellite InSAR volcano observations: Results from the Latin America pilot project. *Journal of Applied Volcanology*, *7*(1), 1–28. https://doi.org/10.1186/s13617-018-0074-0

Saepuloh, A., Aisyah, N., & Urai, M. (2015). Detecting surface structures after large eruption of Mt. Merapi in 2010 using ALOS/PALSAR data. *Procedia Earth and Planetary Science*, *12*, 84–92. https://doi.org/10.1016/j.proeps.2015.03.042

Saepuloh, A., Koike, K., Omura, M., Iguchi, M., & Setiawan, A. (2010). SAR- and gravity change-based characterization of the distribution pattern of pyroclastic flow deposits at Mt. Merapi during the past 10 years. *Bulletin of Volcanology*, *72*(2), 221–232. https://doi.org/10.1007/s00445-009-0310-x

Small, D. (2011). Flattening gamma: Radiometric terrain correction for SAR imagery. *IEEE Transactions on Geoscience and Remote Sensing*, *49*(8), 3081–3093. https://doi.org/10.1109/TGRS.2011.2120616

Solikhin, A., Pinel, V., Vandemeulebrouck, J., Thouret, J. C., & Hendrasto, M. (2015). Mapping the 2010 Merapi pyroclastic deposits using dual-polarization Synthetic Aperture Radar (SAR) data. *Remote Sensing of Environment*, *158*, 180–192. https://doi.org/10.1016/j.rse.2014.11.002

Terunuma, T., Nishida, K., Amada, T., Mizuyama, T., Sato, I., & Urai, M. (2005). Detection of traces of pyroclastic flows and lahars with satellite synthetic aperture radars. *International Journal of Remote Sensing*, *26*(9), 1927–1942. https://doi.org/10.1080/01431160512331326576

Wadge, G., Cole, P., Stinton, A., Komorowski, J. C., Stewart, R., Toombs, A. C., & Legendre, Y. (2011). Rapid topographic change measured by high-resolution satellite radar at Soufriere Hills Volcano, Montserrat, 2008-2010. *Journal of Volcanology and Geothermal Research*, *199*(1–2), 142–152. https://doi.org/10.1016/j.jvolgeores.2010.10.011

Wadge, G., & Haynes, M. (1998). Cover radar images growth of Soufriere Hills Volcano, Montserrat. *International Journal of Remote Sensing*, *19*(5), 797–800. https://doi.org/10.1080/014311698215720

Wadge, G., Saunders, S., & Itikarai, I. (2012). Pulsatory andesite lava flow at Bagana Volcano. *Geochemistry, Geophysics, Geosystems*, *13*(11), 2012GC004336. https://doi.org/10.1029/2012GC004336

Wadge, G., Scheuchl, B., & Stevens, N. F. (2002). Spaceborne radar measurements of the eruption of Soufrière Hills Volcano, Montserrat. *Geological Society Memoir*, *21*(1), 583–594. https://doi.org/10.1144/GSL.MEM.2002.021.01.27

Walter, T. R., Haghighi, M. H., Schneider, F. M., Coppola, D., Motagh, M., & Saul, J., et al. (2019). Complex hazard cascade culminating in the anak krakatau sector collapse. *Nature Communications*, *10*(1), 1–11. https://doi.org/10.1038/s41467-019-12284-5

Walter, T. R., Harnett, C. E., Varley, N., Bracamontes, D. V., Salzer, J., Zorn, E. U., & Thomas, M. E. (2019). Imaging the 2013 explosive crater excavation and new dome formation at Volcán de Colima with TerraSAR-X, time-lapse cameras and modelling. *Journal of Volcanology and Geothermal Research*, *369*, 224–237. https://doi.org/10.1016/j.jvolgeores.2018.11.016

Wang, T., Poland, M. P., & Lu, Z. (2015). Dome growth at Mount Cleveland, Aleutian Arc, quantified by time series TerraSAR-X imagery. *Geophysical Research Letters*, *42*(24), 10614–10621. https://doi.org/10.1002/2015GL066784

Werner, C., Wegmüller, U., Strozzi, T., & Wiesmann, A. (2000). Gamma SAR and interferometric processing software. In: Proceedings of the ERS-ENVISAT Symposium (Vol. 1620, p. 1620).

Williams, R., Rowley, P., & Garthwaite, M. C. (2019). Reconstructing the anak krakatau flank collapse that caused the december 2018 indonesian tsunami. *Geology*, *47*(10), 973–976. https://doi.org/10.1130/g46517.1